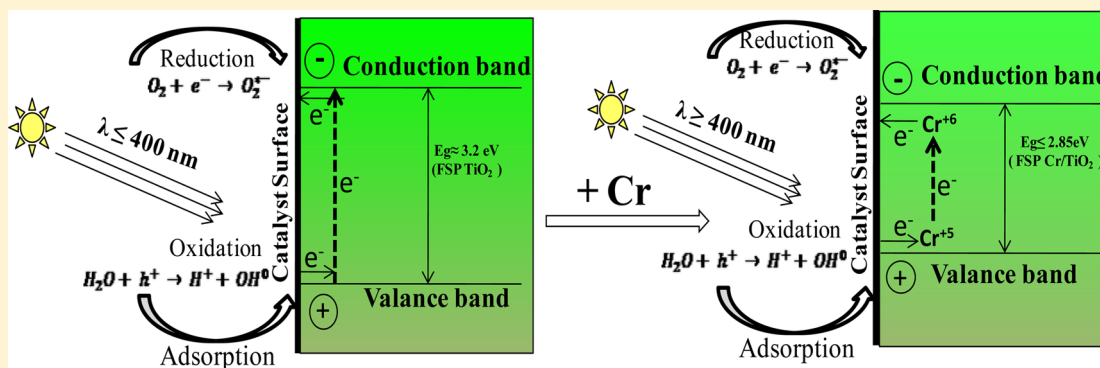


Flame Aerosol Synthesized Cr Incorporated TiO₂ for Visible Light Photodegradation of Gas Phase Acetonitrile

Siva Nagi Reddy Inturi,[†] Thirupathi Boningari,[†] Makram Suidan,^{*,‡} and Panagiotis G. Smirniotis^{*,†}[†]Chemical Engineering Program, School of Energy, Environmental, Biological and Medicinal Engineering, University of Cincinnati, Cincinnati, Ohio 45221-0012, United States[‡]Engineering College and Architecture, American University of Beirut, Beirut 1107-2020, Lebanon

S Supporting Information



ABSTRACT: A series of Cr–TiO₂ nanoparticles with different atomic ratios of Ti to Cr have been synthesized by adopting a one-step flame aerosol synthesis technique. The photocatalytic activity of flame aerosol made TiO₂ loaded with various amounts of Cr was studied as a catalyst for gas phase photodegradation of acetonitrile (ACN) under visible light (400–800 nm). It was found that the optimal concentrations of Cr and TiO₂ exist (Ti/Cr atomic ratio = 40) for the efficient oxidation of ACN in the gas phase. XRD patterns showed a decrease in the anatase phase with increase in the amount of Cr loading. Our H₂–temperature programmed reduction (TPR) results indicate a strong interaction (Cr–O–Ti) between support and dopant in the Cr modified TiO₂ as-synthesized catalysts. Our XPS results illustrated that the relative atomic percentage value of Ti³⁺/Ti⁴⁺ characterized by XPS was significantly high for the Cr/TiO₂ nanoparticles with Ti/Cr = 40 atomic ratio (Ti³⁺/Ti⁴⁺ = 1.14, 42.1%), whereas other samples demonstrated low atomic percentage value of Ti³⁺/Ti⁴⁺ (Ti³⁺/Ti⁴⁺ = 0.18–1.05). Moreover, Cr interacts with the TiO₂ nanostructure in the interface of flame-made nanoparticles, bulk Cr oxide exists over the surface of TiO₂ nanostructure. The photodegradation ability of TiO₂/Cr catalyst with Ti/Cr atomic ratio of 40 was highly related to the existence of Cr⁶⁺ species which strongly interacted with TiO₂. The reduction peaks in Cr-doped TiO₂ shifted to much lower temperatures, due to the increase in the reduction potential of titania and chromium species. The strong interaction (formation of Cr–O–Ti bonds) is the main reason that Cr/TiO₂ is an active photocatalyst in visible light. Among all of the catalysts tested, the system with Ti/Cr atomic ratio 40 demonstrated a superior catalytic performance with the rate constant of 0.812 m³ g⁻¹ mol⁻¹ under visible light irradiation. The proposed route of the catalytic activity of the above material in visible light involves the reaction of dopant level electrons with surface Cr, which makes available valence band holes to perform oxidation reactions.

1. INTRODUCTION

Over the past decades photocatalysis using semiconductor catalysts has drawn considerable academic interest for purification of water and air streams which contains volatile organic contaminants. The photocatalytic degradation of the volatile organic compounds (VOCs) has drawn significant attention because they are inexpensive and nonselective and can be performed at atmospheric pressure and room-temperature.^{1–4} During the photocatalytic process, when light (photons) with sufficient energy is absorbed on the catalyst, it leads to the excitation of the electrons from the valence band to the conduction band, thus generating the electron–hole pairs. The photogenerated holes will form hydroxyl radicals

when they react with the OH⁻/water over the surface of the catalyst. The hydroxyl radicals formed will react with VOCs adsorbed on the photocatalyst's surface to transform the VOCs into minerals (CO₂ and H₂O).

The TiO₂ is widely used as semiconductor in environmental applications due to its resistance to corrosion, nontoxicity, physical and chemical stability, and highly economical. In order to achieve a photocatalytic reaction, it is essential to utilize a light source of satisfactory intensity so as to acquire energy that

Received: April 30, 2013

Revised: December 11, 2013

Published: December 12, 2013

exceeds the TiO₂ band gap energy (E_{bg}). However, the large band gap of the TiO₂ (E_{bg} (anatase) = 3.2 eV, E_{bg} (rutile) = 3.02 eV, and E_{bg} (brookite) = 3.2 eV) requires a wavelength of 400 or less for the excitation of the catalyst.^{5,6} Accordingly, TiO₂ particles can only be activated by ultraviolet light which makes up only ~5% of the solar spectrum, while about 40% of the solar spectrum photons are in the visible region. This limits the commercial potential of titania to serve as effective photocatalyst harvesting solar light. Most researchers and their studies are focused on overcoming these plaguing issues in the photocatalysis by focusing on the surface modifications of titania semiconductor. The basic strategies followed are as follows: (i) to inhibit electrons and holes recombination by increasing the charge separation and thus the efficiency of the photocatalytic process; (ii) to increase the light absorption visible light region; and (iii) to modify the conversions toward the selective product (i.e., by using the combined reactor's which includes recycle reactor's, sono-Fenton, sono-photocatalysis, sono-enzymatic treatments, photo-Fenton techniques, UV/H₂O₂, UV/ozone, ozone/H₂O₂, etc.).⁴ Among the above strategies increasing the wavelength response range to the visible light region has been much sought out due to its potential application for commercial process.

The approach is to dope the semiconductor with a small amount of cations and/or metal oxides in TiO₂ to improve their light absorbance range into the visible region.^{7–10} Although in principle the introduction of cations into TiO₂ is capable of inducing visible light sensitization, they exist mostly as impurities and promote charge recombination. Hence, no noticeable enhancement in photocatalytic activity could be observed for these catalysts under visible light illumination.^{11,12} The incorporation of transition metal/metal oxides in the TiO₂ crystal lattice will result in the development of new energy levels between valence band (VB) and conduction band (CB), thus prompting a shift of light absorption toward the visible light region. The nature and the amount of doping agent have a significant effect on photocatalytic activity. Studies have shown that high energy implantation of metal cations (V, Cr, Fe, Co, and Ni) into the TiO₂ matrix^{13–16} and resulted in photocatalytic activation under visible light with 25–32% solar light absorption.

Conventional wet synthesis in typical laboratory-size glassware is still easy to handle, but it may not be the case at industrial level production. The low yield in addition to the long processing time, especially for very fine and pristine nanoparticles, necessitate the need for large tanks and high energy equipment which in turn limits its flexibility in direct scaling-up. Moreover, these methods also incur additional costs in terms of production time, high energy consumption, floor space, and waste disposal, which subsequently reflect in the price of final products. The flame aerosol technique is an established synthesis technique capable of producing inexpensive nanoparticles on an industrial scale.^{17–21} Liquid spray flame pyrolysis (LFSP) synthesis technique has the benefit of being able to utilize a broader spectrum of liquid precursors so that even noble metal deposited TiO₂ can be made in one step.¹⁸

In the present study, Cr-doped TiO₂ photocatalysts are synthesized using a flame spray pyrolysis (FSP) technique.^{20,21} The liquid-to-particle synthesis by FSP facilitates the synthesis of homogeneously doped materials. The photocatalytic activity of different amounts of Cr doped TiO₂ are specifically evaluated for gas phase visible light photocatalytic degradation of

acetonitrile. Acetonitrile is chosen as the model organic compound for the photocatalytic oxidation studies due to its molecular simplicity and because it is frequently found in various civil and industrial wastewaters.²² Acetonitrile is noticed as an in-door air pollutant which is emitted by polymeric materials, resins, and smoking tobacco. It is also a frequently encountered degradation intermediate of many complex organic pollutants. Acetonitrile is a very attractive model molecule for photo-oxidation studies because it is a simple molecule which contains an alkyl and cyanide group that would undergo dissimilar oxidation routes.

2. EXPERIMENTAL SECTION

2.1. Catalysts Preparation. The detailed synthesis procedure for the flame-made nanoparticles is explained in detail in our previous studies.^{20,21} Briefly, a mixture of *o*-xylene (Sigma–Aldrich Reagent, 99%)/acetonitrile (Sigma–Aldrich Reagent) in the volume ratio of 3/1 is used as the solvent. For pure FSP made titanium-tetra-isopropoxide (TTIP, Sigma–Aldrich, purity N97%) which was used as precursor and diluted with the solvent to a 0.5 M solution, metal oxide nanoparticles were synthesized by a one-step FSP synthesis technique. Precursor solutions resulting in powders of chromium incorporated TiO₂ were prepared by dissolving predetermined amounts of TTIP and chromium precursor (Chromium(III) 2-ethylhexanoate, Strem, 70% in mineral spirits Cr) to make different atomic ratios of Ti/Cr (∞ , 100, 75, 50, 40, 30, 20, and 10). The total molar concentration of Ti + Cr in the liquid precursor was set at 0.5 M. In the course of LFSP, the liquid precursor was introduced through a spray nozzle at a flow rate of 3 mL min⁻¹ using a syringe pump (Cole Parmer, 74900 series), where it was dispersed by a surrounding 5 L min⁻¹ flow of O₂ (1.5 bar, Wright Brothers, 99.98%). Ignition of the dispersed droplets was ignited by an adjacent supporting flame (premixed 1.0 L min⁻¹ O₂/1.0 L min⁻¹ CH₄). Additionally, 3 L/min sheath O₂ (BOC Gases) was issued through the outermost sintered metal ring. The nanoparticles leaving the flame were collected on a flat glass fiber filter (Whatman GF/A, 150 mm in diameter) aided by a vacuum pump (Grainger Inc.). The synthesized nanoparticles were scraped from the filter for direct use as catalyst without any additional treatment. The metal components of the catalysts are denoted Ti/Cr.

2.2. Characterization. **2.2.1. BET Measurements.** The Brunauer, Emmett, and Teller (BET) specific surface area, pore diameter, and pore volume of the catalyst were determined from the nitrogen adsorption equilibrium isotherm at liquid nitrogen temperature (77 K) using an automated gas sorption system (Micromeritics ASAP 2010) operating in continuous mode. Prior to the analysis, 0.050 ± 0.005 g of catalyst was evacuated under helium atmosphere for 3 h at 250 °C in the degassing port of the instrument. The adsorption isotherms of nitrogen were gathered at 77 K using relative pressure ranging from 0.05 to 0.99 and by taking 0.162 nm² as the molecular area of the nitrogen molecule.

2.2.2. X-ray Diffraction. Powder X-ray diffraction (XRD) measurements were employed for the identification of phases of the as-synthesized Cr-incorporated TiO₂. The XRD patterns were recorded on a Phillips Xpert diffractometer using nickel-filtered Cu K α (wavelength 0.154056 nm) radiation source and a scintillation counter detector. An aluminum holder was used to support the catalyst samples. The intensity data were composed over a 2θ range of 10°–80° with a step size of 0.025° and a step time of 0.50 s. Crystalline phases were recognized by

Table 1. Characterization Results for Cr Incorporated TiO₂ Made by Flame Aerosol Pyrolysis Method

catalyst	surface area analysis					X-ray diffraction analysis			
	isotherm type ^a	SSA (m ² /g)	d_{BET}^b (nm)	pore volume (cm ³ /g)	pore diameter (nm)	X_{Anatase}^c (%)	d_A^d (nm)	d_R^d (nm)	D_{XRD}^e (nm)
P25		51	30	0.18	15	80	30	158	56
FSP TiO ₂	II	109	14	0.41	14	81	27	130	46
100	II	99	15	0.26	10	75	23	120	47
75	II	97	16	0.43	17	75	21	91	39
50	II	96	16	0.31	14	70	26	114	53
40	II	93	16	0.30	14	71	24	122	52
30	II	91	17	0.29	13	59	31	107	63
20	II	88	17	0.28	13	57	31	90	57
10	II	83	18	0.21	10	44	25	127	82

^aIsotherm type is based on IUPAC nomenclature. ^b d_{BET} is the mass weighted average particle diameter. ^c $X_{\text{Anatase}} (\%) = 100 - X_{\text{Rutile}} (\%)$. ^d d_A and d_R are the crystallite sizes of anatase and rutile, respectively. ^e D_{XRD} is calculated based on mass weight average density of anatase and rutile phases determined by XRD.

comparison with the reference data from International Center for Diffraction Data (ICDD) files.

2.2.3. UV-vis Spectroscopy. The catalyst powders were characterized by UV-vis spectrophotometer (Shimadzu 2501PC) with an ISR1200 integrating sphere attachment for their diffuse reflectance with the wavelength ranging from 200 to 900 nm. BaSO₄ was used as the standard for these measurements.

2.2.4. Transmission Electron Microscopy (TEM). Selected fresh catalyst samples were characterized with a Philips CM 20 electron microscope. The samples were sonically dispersed in isopropyl alcohol and transferred into a carbon-Cu grid, and after complete evaporation of the isopropyl alcohol, the particles attached on the walls of holes in the carbon film were examined. The applied accelerating voltage was 200 keV, with a LaB₆ emission current and a point-to-point resolution of 0.27 nm.

2.2.5. Temperature Programmed Reduction (H₂-TPR). H₂-TPR of as-prepared aerosol nanoparticles was performed using an automated catalyst characterization system (Micromeritics model AutoChem 2910). Prior to the analysis approximately 0.050 g of the catalysts were pretreated at 200 °C for 2 h in ultra high pure helium (30 mL min⁻¹) stream. A mixture of isopropanol and liquid nitrogen was used in the trapper to collect the formed water during the TPR experiment. After preheating, samples were tested by increasing the temperature from 50 to 800 °C. The temperature was then kept constant at 800 °C until the signal of hydrogen consumption returned to the initial values. The temperature programmed reduction runs were carried out with a linear heating rate (10 °C/min) in a flow of 10% H₂ in argon with a flow rate of 20 mL min⁻¹. The hydrogen consumption was measured quantitatively by a thermal conductivity detector.

2.2.6. X-ray Photoelectron Spectroscopy (XPS). The as-prepared aerosol nanoparticles were investigated by X-ray photoelectron spectroscopy (XPS) experiments on a Pyris-VG thermo scientific X-ray photoelectron spectrometer system equipped with a monochromatic Al K α (1486.7 eV) as a radiation source at 300 W under UHV (6.7×10^{-8} Pa). Sample charging during the XPS measurement of as-synthesized Cr-incorporated TiO₂ samples was compensated by an electron flood gun. The electron lift off angle was 45° with respect to the sample surface. The spectra were recorded in the fixed analyzer transmission mode with pass energies of 89.45 and 35.75 eV for recording survey and high resolution spectra, respectively. The powdered catalysts were mounted onto the sample holder and

evacuated overnight at room temperature at a pressure on the order of 10⁻⁷ Torr.

2.3. Photocatalysis. The photocatalytic reactor employed for the gas-phase photocatalytic degradation and photolysis in this study was described in detail in the Supporting Information (Figures S1 and S2). In short, all tubing used was made of stainless steel 316. Zero grade air (99.9%) from a cylinder was passed through mass-flow controller (MKS). A 74900 Cole-Parmer liquid infusion syringe pump was employed to inject liquid acetonitrile into the air stream at the appropriate rate. The resultant gas mixture entered into the photocatalytic reactor placed into a photochemical safety cabinet for protection of personnel from UV light. The photocatalytic reactor is made of quartz tube with an inner diameter of 6 mm and length of 1 ft. Six 8 W fluorescent white light lamps (Wiko F8T5W) were used as the visible light source. Along with plastic housing coated with aluminum foil for better use of light. Acrylite OP2 sheets were used to filter UV light. The cooling jacket around the reactor effectively precluded the IR part of the spectra from penetrating into the reactor and helps in cooling the lamps along with maintaining constant reactor temperature. The as-prepared FSP TiO₂, P25, and Cr-incorporated TiO₂ nanoparticles were deposited onto the internal surface of the reactor by using the 5 wt % of catalyst slurry in distilled water. The reactor vessel was continually rinsed with catalyst slurry with every rinse followed by drying at 120 °C for 120 min. The weighted catalyst was 0.06 g corresponding to the catalyst loading of 1.04 mg of TiO₂ per cm² of irradiated reactor surface. The probe chemical (acetonitrile) was mixed with water in 1:3 volume ratios. Appropriate flow of air was maintained through the inlet of the reactor. The liquid reactant was fed through a spray nozzle at a flow rate to maintain the concentration of the inlet to the reactor as 500 ppm using a syringe pump (Cole Parmer, 74900 series). A small portion of the mixing section before inlet of the reactor was kept at 150 to vaporize the liquid reactant. The temperature in the reactor was determined by heat release of the lamps and varied from 30 °C at the reactor bottom to 35 °C at the reactor top. The reactor effluent is directed into a gas-sampling valve of a QP5050A GC-MS (Shimadzu) to analyze the products.

3. RESULTS AND DISCUSSION

3.1. BET Surface Area, Pore Size, and Pore Volume.

The BET surface area, pore diameter, pore volume, and particle diameter of the photocatalyst are shown in Table 1.

The specific surface area decreased with Ti/Cr atomic ratio changing from 100 to 10. The BET surface area of pure TiO₂ (109 m²/g) is much higher than commercial Degussa P-25 (50 m²/g). We have investigated the N₂ adsorption/desorption isotherm studies for the selected flame made samples (20, 30, and 40 Ti/Cr and TiO₂). The representative results are now shown in Figure 1. To determine the porous structure of the

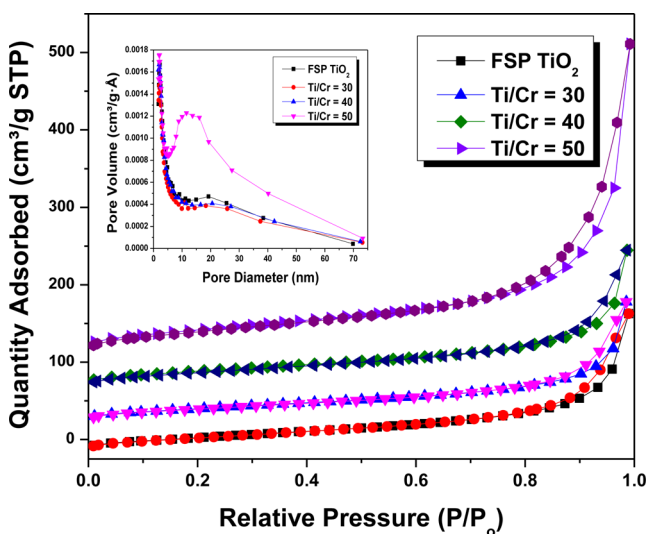


Figure 1. Nitrogen adsorption and desorption isotherms for selected flame made samples (30, 40, and 50 Ti/Cr and FSP TiO₂). (Insert) Pore size distribution of as-prepared 30, 40, and 50 and TiO₂ samples, respectively.

catalysts nitrogen adsorption and desorption isotherms at 77 K were investigated. The nitrogen adsorption–desorption isotherms of 20, 30, and 40 Ti/Cr and TiO₂ samples fit in to type II isotherm with an H3 type hysteresis loop,^{23–25} which is a characteristic of mesoporous nature of the corresponding materials. These catalysts showed an adsorption–desorption hysteresis cycle which can be attributed to capillary condensation in mesoporous solids. It is understood that this type of loop, exhibiting no limiting adsorption at high P/P_0 , comes from the congregation of loosely coherent particles. One can observe from the figure that the catalyst undergoes a monotonical increase in the adsorbed volume at a high relative pressure followed by plateau, which is in turn a characteristic of solid micropores. The type H3 loop is associated with narrow slit-like pores.²⁶ Some other researchers also observed similar adsorption and desorption isotherms for the nanoporous materials.^{24,25} The poresize distribution results revealed that the Cr-incorporated flame made TiO₂ samples showed significant differences with increase in Ti/Cr atomic ratio (Figure 1, insert). The surface tridimensional structure of the mesoporous materials leads to the facile adsorption/desorption equilibrium and better mass transfer for the reactants and products hence improves the catalytic activity of the materials in the photocatalytic applications.

3.2. XRD Characterization. Figure 2 shows the large angle powder X-ray diffraction patterns of various amounts of Cr modified titania. The diffractogram patterns of pure TiO₂ (Degussa P25) are also presented for comparison purposes. For the FSP titania's and the P25 sample, the strong characteristic peaks of titania (typically at $d = 3.54, 1.90,$ and 2.40 \AA , which correspond to anatase phase (JCPDS no. 21–

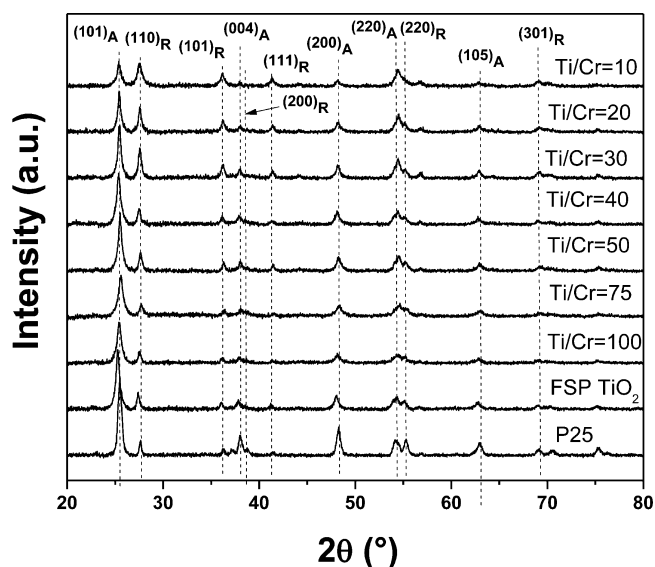


Figure 2. Powder X-ray diffraction patterns of Cr doped titania catalysts made by FSP with different Ti/Cr ratios; (A → anatase and R → rutile TiO₂).

1272)) can be observed. In order to compare the effects of Cr doping on the anatase-rutile phase transformation, the fraction of rutile, X_R was calculated from the respective peak intensities using the following equation:

$$X_R \% = \left(1 - \frac{1}{1 + \frac{1.26I_R}{I_A}} \right) \times 100 \quad (1)$$

where I_R and I_A are the X-ray intensities of the rutile (110) and anatase (101) peaks, respectively. These relative rutile and anatase fractions are listed in Table 1. The rutile fractions of P25 and FSP TiO₂ were estimated from eq 1 to be 19% of the FSP TiO₂, and Cr-incorporated TiO₂ samples exhibited increase in the rutile fractions with increase in the amount of Cr incorporated to the flame-made TiO₂ nanoparticles. No characteristic peak of chromium oxides (Cr₂O₃ and CrO₂) was found in the XRD patterns.

These results suggest that the doping levels we employed did not induce the formation of discrete impurity phases and that the Cr ion appears to have been integrated into the basic structure of TiO₂. However, it is conceivable that metal impurities, which were formed during synthesis dispersed on the surface. Thus, the crystal structure of TiO₂ indicates a mixture of anatase and rutile for all the as-synthesized metal-doped TiO₂ samples. Therefore, it is interesting to note that the Cr doping promoted the anatase to rutile phase transformation of TiO₂.

The X-ray powder diffraction patterns are also used to determine the crystallite size of all the prepared samples. The crystallite size τ is determined from the broadening of the peaks by Scherrer's formula.²⁷

$$\tau = \frac{K\lambda}{\beta_\tau \cos \theta} \quad (2)$$

where K the shape factor = 0.9; β_τ is the width of the peak at half the maximum intensity (fwhm) after subtraction of instrumental noise, and 2θ is the diffraction angle. The estimation shows that the mean crystal size of the initial

anatase TiO_2 individual particles calculated from eq 2 was 46–80 nm.

X-ray diffraction pattern of P25 and chromium doped TiO_2 nanoparticles are shown in Figure 2. The diffraction pattern corresponds to the mixed (anatase + rutile) phases of TiO_2 . A close inspection of the intense (1 0 1) peak reveals that doping of chromium shifts the diffraction peaks slightly to lower angle. In octahedral coordination, the ionic radii of different valence states of chromium are Cr^{3+} (0.75 Å), Cr^{4+} (0.69 Å), Cr^{5+} (0.63 Å), and Cr^{6+} (0.58 Å), respectively.²⁸ In TiO_2 , Ti^{4+} is surrounded by six oxygen ions and has an ionic radius of 0.74 Å. The (101) peak is shifted to lower or higher angle in Cr-doped TiO_2 samples, indicating the distortion of TiO_2 crystal lattice by the chromium doping. This is possible only when Cr species substitutes Ti^{4+} , since the ionic radii of Cr species is different than that of Ti^{4+} . Earlier, TiO_2 lattice distortion was ascribed to the substitution of titanium ion with dopant ion because the ionic radius of dopant was slightly smaller than that of Ti^{4+} .^{29,30} However, this shift is also evident in the pure FSP TiO_2 . It suggests that the Ti^{3+} substitutes Ti^{4+} and leads to the increase of lattice size, since the ionic radii of Ti^{3+} (0.81 Å) is larger than that of Ti^{4+} (0.74 Å).³¹ The crystallite sizes of pure and doped TiO_2 nanoparticles are determined using the Scherrer's equation. The calculated crystallite sizes are given in Table 1. As we can see, the crystallite size decreases with dopant concentration. The decrease in crystallite size indicates an increase in structural defects that prevent grain growth. As the XRD pattern shows the reduction in the intensity of the (101) plane diffraction peak with an increase in chromium loading (Figure 2). Since the ionic charge of Cr species is different from that of Ti^{4+} , doping of Cr generates oxygen vacancies in the lattice of TiO_2 to maintain charge neutrality. As we increase the doping of Cr, a few numbers of oxygen vacancies either move to the interstitial position or to the surface and grain boundary regions. These structural defects affect the crystallinity of the material and results in the reduction of the peak intensity and prevent the growth of the crystallite. We have not detected any impurity diffraction peaks which indicate that most of the dopants have entered into the TiO_2 lattice. However, fractions of chromium related impurity phases may be present on the surface or on grain boundary which may be beyond the detection limit of XRD.

3.3. UV–vis Spectra. As shown in Figure 3, UV and visible light with a wavelength less than 550 nm can be absorbed by Cr– TiO_2 materials. The light absorbance increases with the Cr concentration in the sample.

One can also observe a shoulder peak at about 430 nm for the catalyst samples with $\text{Ti}/\text{Cr} = 100, 75, 50, 40, 30, 20,$ and 10 which corresponds to the existence of Cr^{6+} . This peak is less apparent in the case of $\text{Ti}/\text{Cr} = 30, 20,$ and 10.³² Degussa P25 TiO_2 is characterized by sharp absorption edges at about 390 nm ($E_g \approx 3.15$ eV).

However, the FSP TiO_2 has the absorption of about 397 nm ($E_g \approx 3.12$ eV). The enhanced absorptions in the range from 400 to 650 nm with the increasing Cr content, accompanied with the changes on color from white to yellow.³² The decreases in the band gap is also affected by the change in the ratio of anatase to rutile phase of the TiO_2 ; as we increase the amount of Cr the rutile phase increased as given in Table 1. The enhanced absorption observed for the Cr– TiO_2 samples in the visible region can be considered to involve the excitation of the 3d electrons of the Cr ion to TiO_2 conduction band

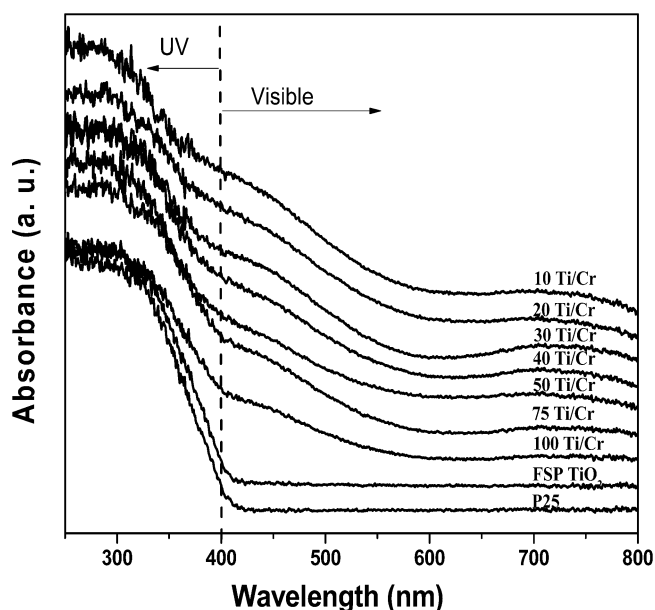


Figure 3. UV–vis diffuse reflectance spectra of Cr doped titania catalysts made by FSP with different Ti/Cr ratios.

according to their respective energy levels.^{29,33,34} As the amount of Cr increased in the catalyst, there was not much improvement (change in band gap was from 2.85 to 2.46) in the absorption wavelength of the sample. The generation of new energy levels due to the injection of impurities into the TiO_2 lattice coupled with the generation of oxygen vacancies by Cr ion doping may contribute to the observed visible-light absorption of the Cr– TiO_2 samples.

3.4. Transmission Electron Microscopy (TEM). Figure 4 shows TEM images of Cr/ TiO_2 nanocrystals with different

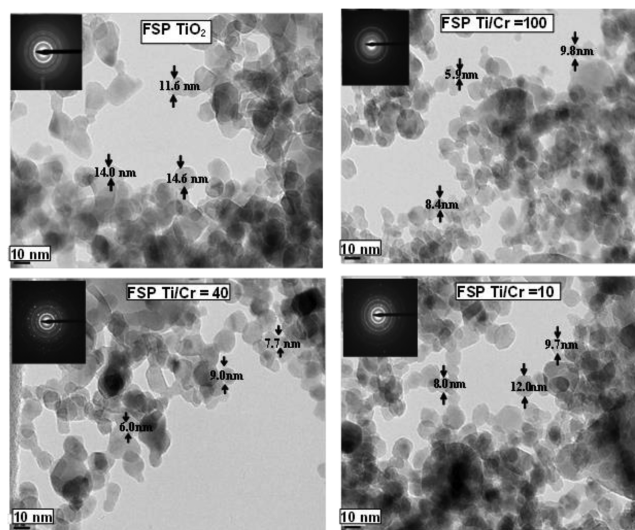


Figure 4. TEM images of as-prepared FSP-made Cr-doped TiO_2 based catalysts.

amounts of Cr loading on TiO_2 . In terms of particle shapes, the FSP-made Cr/ TiO_2 nanocrystals and pure TiO_2 consists of irregular particles with round edges. The particle size of pure TiO_2 was 14.6–11 nm which in agreement with the BET particle diameter, whereas the particle sizes of the Cr/ TiO_2 are lower than the diameters of the particles predicted from BET or

XRD data. Despite the consistency of various characterization techniques as discussed above, the solubility limit of FSP-made Cr/TiO₂ remains rather ambiguous. Formation of a new Cr phase could not be detected from XRD even at low Ti/Cr ratio, presumably due to the well dispersed and small segregated Cr grains.

3.5. Temperature-Programmed Reduction (H₂-TPR).

The TPR profiles and total hydrogen consumption for all the chromium incorporated TiO₂ materials are given in Figure 5

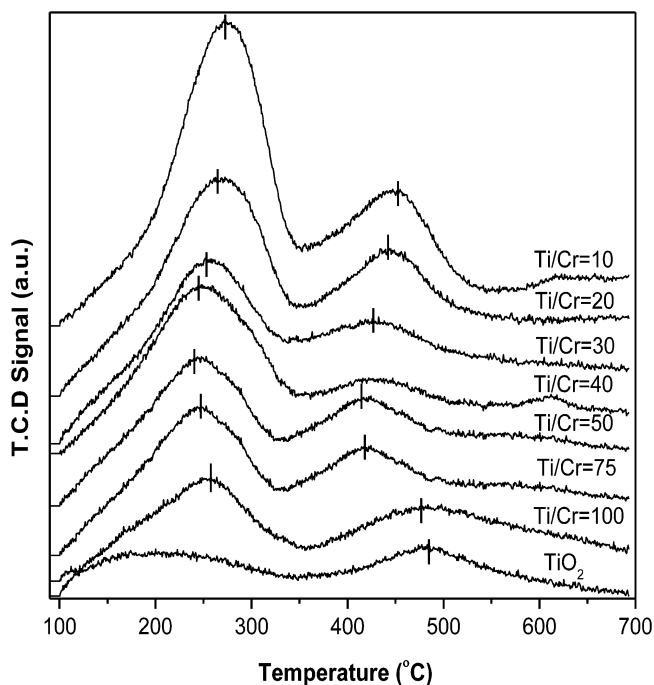


Figure 5. H₂-TPR patterns of Cr doped titania catalysts made by FSP with different Ti/Cr ratios.

and Table 2, respectively. The reduction profiles of bulk CrO₃ comprise of the reduction peaks at 280, 462, and 585 °C. These peaks can be ascribed to the stepwise reduction of Cr⁶⁺ → Cr⁵⁺, Cr⁵⁺ → Cr³⁺, and Cr³⁺ → either Cr²⁺ or the metallic state, respectively.³⁵ As shown in Figure 5 and Table 2, FSP TiO₂ shows two peaks at 216 and 480 °C which can be ascribed to

Table 2. H₂-Temperature Programmed Reduction and Hydrogen Consumption of Cr Metal Incorporated TiO₂ Catalysts with Various Ti/Cr Atomic Ratios Obtained at Different Temperatures

catalyst ^a	TPR reduction transitions				H ₂ consumption (μ mol/ g of catalyst)
	T ₁ (°C)	T ₂ (°C)	T ₃ (°C)	T ₄ (°C)	
FSP TiO ₂	201	484			60.2
100	255	426	435	525	1425
75	236	410	419	468	1460
50	229	398	409		1605
40	209	387	403		2060
30	228	393	410		2179
20	232	409	423	443	2307
10	248	415	446	456	2560

^aTiO₂ and Cr-TiO₂ as-prepared nanoparticles with respect to Ti/Cr atomic ratio.

the partial reduction of TiO₂. In the case of Cr-incorporated TiO₂ samples, the low temperature reduction peaks T₁ and T₂ appear at around 157 to 275 °C, which can be attributed to the partial hydroxylation and reduction of TiO₂ along with the reduction of Cr⁶⁺ to Cr⁵⁺, respectively.¹¹ As one can observe in Figures 5 and S3, the two reduction peaks (T₁ and T₂) were overlapped in the H₂-TPR profile of Cr-doped TiO₂ catalysts, which is due to the strong interaction of TiO₂ with the chromium oxide species. This is a clear indication to suggest that the Cr incorporation is promoting the catalyst for the partial reduction of Ti⁴⁺ to Ti₄O₇. Our TPR results are in good agreement with our XPS results, where the Cr–O–Ti bonding was established by the shift in the binding energies. The low temperature reduction peak height and area increase with decrease in Ti/Cr atomic ratio from 100 to 10. The interaction between Cr species and TiO₂ led to the increase in the reduction potential of the active species and broadened the temperature window for reduction.

The appearance of the number of reduction transition peaks of these materials depends on the Cr concentration and the interaction between Cr and TiO₂. It is highly difficult to distinguish the overlapped peaks without deconvolution of the peak. Therefore, overlapped reduction peaks were deconvoluted into several sub-bands by searching for the optimal combination of Gaussian bands with the correlation coefficients (*r*²) above 0.99. One can clearly observe from the deconvoluted spectra that there are 3–4 reduction peaks in the TPR profiles of Cr–TiO₂ samples with a Ti/Cr ratio from 100 to 10. In particular, Cr/TiO₂ samples with Ti/Cr atomic ratios of 100, 20, and 10 show only three reduction peaks which can be ascribed to the reduction of Ti⁴⁺ to Ti₄O₇, Cr⁶⁺ to Cr⁵⁺, and Cr⁵⁺ to Cr³⁺. Consequently, Cr/TiO₂ samples with Ti/Cr atomic ratios of 75, 50, 40, and 30 show four reduction peaks which can be ascribed to the reduction of Ti⁴⁺ to Ti₄O₇, Cr⁶⁺ to Cr⁵⁺, Cr⁵⁺ to Cr³⁺, and Cr³⁺ to Cr²⁺.

For the TiO₂/Cr (Ti/Cr = 100, 75, 50, 40, and 30) materials, the number of Ti atoms are much higher than that of Cr, each of the Cr ions present in these materials can interact with the TiO₂ loaded on the surface inside TiO₂/Cr pores. However, this surface layer of TiO₂ stops a fraction of Cr in the framework from being reduced by H₂ as indicated by the decrease of peak intensity in TPR. In other words, the total H₂ consumption increased monotonically with the increase in Cr loading in the Cr–TiO₂ samples (Table 2).

The total area of the low temperature peak monotonically increased along with the increase in the Cr loading in the sample, and this area indicates the interaction of Cr with Ti. The samples with Ti/Cr ratios from 100, 75, 20, and 10 have two distinctive peaks. The second (high temperature) peak of these catalysts has a significant area which can be attributed to the reduction of surface Cr⁵⁺ and Cr³⁺ species. Among all of the catalysts, Cr/TiO₂ catalysts with a Ti/Cr atomic ratio of 40 showed high intense Cr⁶⁺ to Cr⁵⁺ reduction peaks and low intense Cr³⁺ to Cr²⁺ reduction peaks along with the reduction of Ti⁴⁺ to Ti₄O₇. The low temperature reduction peak is shifted to lower temperatures in the Cr–TiO₂ as-synthesized catalysts with Ti/Cr atomic ratios of 50, 40, and 30 which implies that the reduction potential of surface Cr and Ti species and the interaction between Ti and Cr significantly increased in these catalysts. The strong interaction (formation of (Cr–O–Ti) bonds) and the increase in reduction potential seem to be the reason for the high activity of as-prepared Cr/TiO₂ photocatalyst under visible light irradiation.¹⁶ These results are in

good agreement with our XPS studies where the strong interaction of Cr and TiO₂ established by the electrons migrate from the TiO₂ nanoparticles to chromium species.

The total hydrogen consumed of the first peak of the catalyst samples during TPR studies increased monotonically with the decrease in Ti/Cr atomic ratio (from 100 to 10).

As can be seen from Figure 6, the intensity of the low temperature peak monotonically increased with chromium

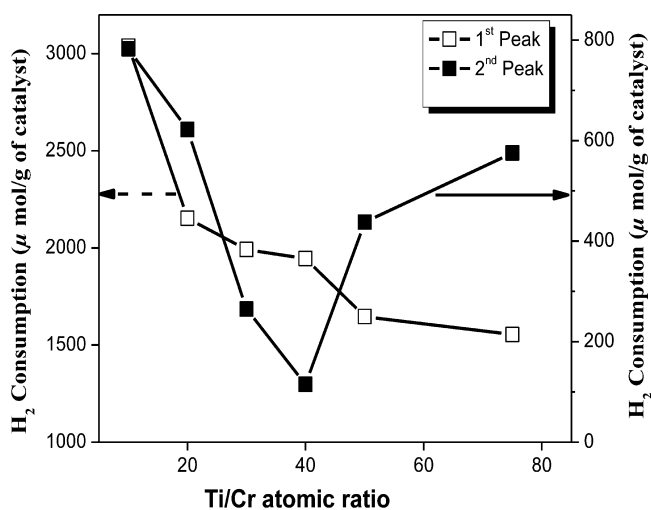


Figure 6. H₂-consumption for 1st and 2nd peaks of Cr doped titania catalysts made by FSP with different Ti/Cr ratios.

species loading which indicates the increasing amount of Cr⁶⁺ species. It is interesting to note that the intensity of the second peak reached a minimal H₂ consumption with the Ti/Cr atomic ratio of 40. Further increase in the chromium content led to the increase in the intensity of the high temperature peak. These results indicate that the reducibility of Cr⁶⁺ species increased and the reducibility of Cr³⁺ species decreased in the Cr-incorporated TiO₂ catalyst with a Ti/Cr atomic ratio of 40. Our TPR results are in good agreement with our XPS analysis where the strong interaction between TiO₂ and Cr species (Cr–O–Ti) was established by shift in the binding energies.

3.6. X-ray Photoelectron Spectroscopy (XPS). In order to get insights into the oxidation state of titanium oxide, relative atomic percentage of Ti³⁺/Ti⁴⁺ and to ensure the chemical compositions (Ti/Cr) of the surface layer, the XPS spectra of the as-synthesized Cr/TiO₂ nanoparticles were recorded. For the identification of the titanium oxide phases and the relative percentages of Ti⁴⁺, Ti³⁺ species, the overlapped Ti 2p peaks were deconvoluted into a number of peaks by searching for the optimal combination of Gaussian bands with the correlation coefficients (*r*²) above 0.99 (PeakFit, version 4.0.6). The deconvoluted peaks are designated as specific Ti⁴⁺ and Ti³⁺ species in each spectrum (Figure 7). The relative atomic percentages of Ti³⁺/Ti⁴⁺, Ti³⁺/Tiⁿ⁺, and Ti/Cr species were calculated by the area ratio of the corresponding characteristic peaks. The results are listed in Table 3, and using the XPS peak fitting program, the XPS peak for Ti 2p of the Cr-doped TiO₂ flame-made nanoparticles further divided into two different peaks, one centered on 458.9 ± 0.1 eV, attributed to Ti⁴⁺ species, and the other centered on 458.1 ± 0.1 eV, ascribed to Ti³⁺ species.^{36–39} The relative atomic percentage value of Ti³⁺/Ti⁴⁺ characterized by XPS was significantly high for the Cr/TiO₂ nanoparticles with Ti/Cr = 40 atomic ratio (Ti³⁺/Ti⁴⁺ =

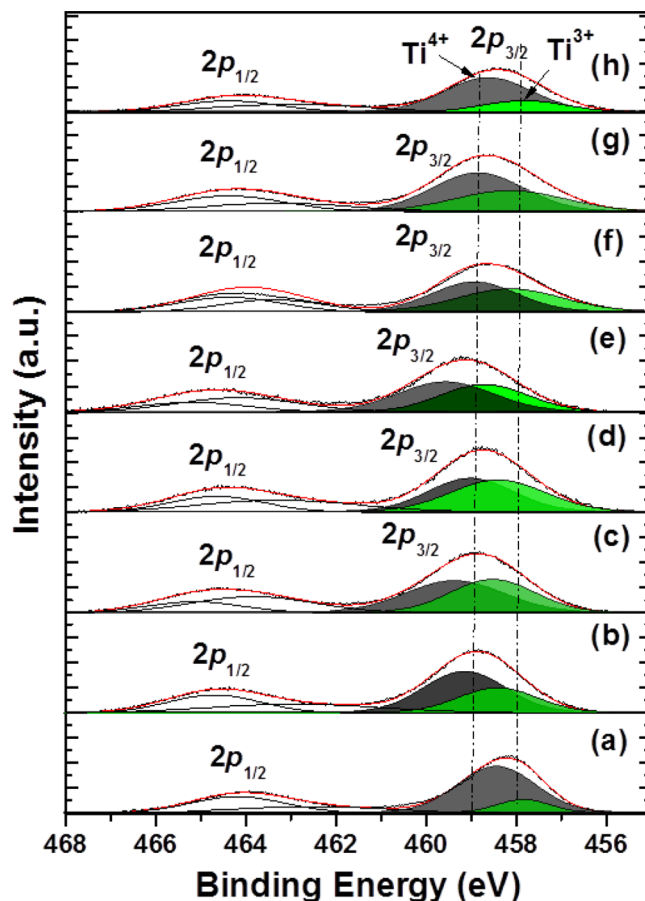


Figure 7. Deconvoluted Ti 2p (XPS) spectra of (a) TiO₂ (b) 10 Ti/Cr, (c) 20 Ti/Cr, (d) 30 Ti/Cr, (e) 40 Ti/Cr, (f) 50 Ti/Cr, (g) 75 Ti/Cr, and (h) 100 Ti/Cr as-prepared flame-made nanoparticles.

1.14, 42.1%), whereas other samples demonstrated a low atomic percentage value of Ti³⁺/Ti⁴⁺ (Ti³⁺/Ti⁴⁺ = 0.18–1.05). It is remarkable to note that the existence of Ti³⁺ species with a narrow band gap is highly beneficial for the promotion of visible light-induced photocatalytic activity.^{40,41} The peak position for Ti 2p in the Cr/TiO₂ sample shifts to higher binding energies than that of bare TiO₂ (Figure 7).

This shift suggests that a lower electron density of the TiO₂ surface after chromium nanoparticles incorporation, this occurrence indicates a strong interaction between Cr species and flame-made TiO₂ nanoparticles in Cr/TiO₂ FSP catalyst with Ti/Cr atomic ratio equal to 40. To compensate for charging effects, which were observed as much as up to +6.72 eV for the Cr-incorporated TiO₂ as-synthesized samples, binding energies were normalized with respect to the position of the C 1s signal determined from of a 5 scans spectrum and held constant at 284.6 eV. Acquisition parameters used for the flame made aerosol (TiO₂ and Cr-TiO₂ systems) materials were 40 scans for the Cr 2p doublet region to obtain data to facilitate analysis due to the low concentration of chromium present.

On the other hand, core level binding energies of Cr 2p_{3/2} and Cr 2p_{1/2} are expected to be 576.9 and 587.0 eV, respectively.⁴² As can be seen from Table 3 and Figure 8, the position of the Cr 2p peaks shifted to lower binding energies compared to the actual binding energies. In particular, Cr/TiO₂ sample with Ti/Cr atomic ratio 40 shows high shift toward lower binding energy. This indicates that the electrons migrate

Table 3. Binding Energy, Surface Atomic Ratios of $\text{Ti}^{3+}/\text{Ti}^{4+}$, $\text{Ti}^{3+}/\text{Ti}^{n+}$, $\text{Ti}^{4+}/\text{Ti}^{n+}$, and Ti/Cr for Cr–TiO₂ (Ti/Cr Atomic Ratio = 100, 75, 50, 40, 30, 20, and 10) As-Prepared Catalysts Determined from Deconvoluted XPS Spectra

catalyst ^a	binding energy (eV)							
	O 1s	Ti 2p		Cr 2p ^b		$\text{Ti}^{3+}/\text{Ti}^{4+c}$	$\text{Ti}^{3+}/\text{Ti}^{n+c}$	$\text{Ti}^{4+}/\text{Ti}^{n+c}$
		Ti 2p _{3/2}	Ti 2p _{1/2}	Cr 2p _{3/2}	Cr 2p _{1/2}			
TiO ₂	429.9	458.3	463.8			0.18	0.09	0.53
100 Ti/Cr	530.2	458.4	463.9	577.2	586.2	0.32	0.15	0.48
75 Ti/Cr	530.3	458.6	464.0	577.1	586.4	0.45	0.20	0.45
50 Ti/Cr	530.2	458.5	464.0	576.5	586.3	0.93	0.22	0.24
40 Ti/Cr	530.4	459.4	464.5	576.3	586.0	1.14	0.34	0.30
30 Ti/Cr	530.4	458.7	464.2	576.4	586.0	1.05	0.32	0.31
20 Ti/Cr	530.5	458.7	464.3	576.5	586.2	0.89	0.31	0.35
10 Ti/Cr	530.1	458.8	464.4	576.8	586.3	0.57	0.22	0.39

^aFlame spray pyrolysis assisted catalysts. ^bBinding energy of Cr with various Ti/Cr atomic ratio. ^cRelative amounts are according to the metal atomic percentages surface elemental composition determined by XPS; $\text{Ti}^{n+} = (\text{Ti}^{4+} + \text{Ti}^{3+})$

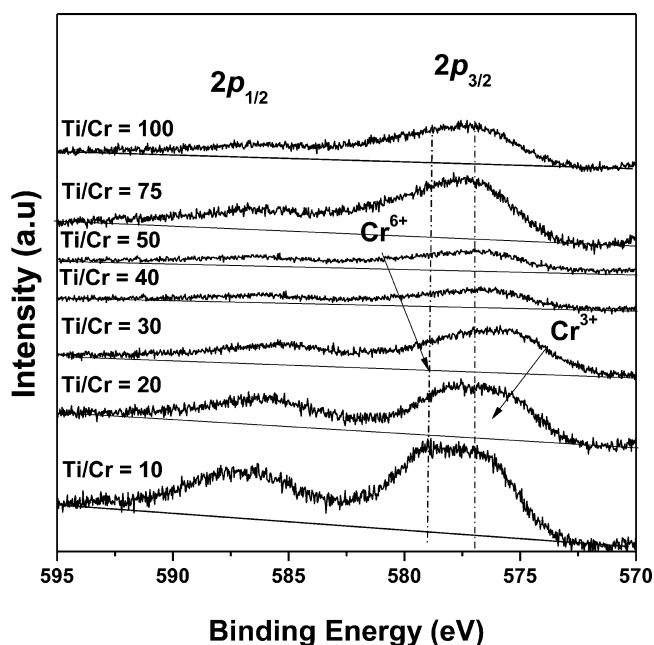


Figure 8. Cr 2p XPS spectra of Cr–TiO₂ (Ti/Cr atomic ratio = 10, 20, 30, 40, 50, 75, and 100) as-prepared flame-made nanoparticles.

from the TiO₂ nanoparticles to chromium species, which suggests a strong interaction between Cr and TiO₂ nanostructure in the interface of flame-made nanoparticles. The increase in the concentration of chromium species up to 40 Ti/Cr atomic ratios monotonically increased the interaction between TiO₂ and dopant. Further increase in the concentration of Cr led to the weak interaction with the titania. These results clearly imply that Cr species have been strongly incorporated into TiO₂ lattice with this optimized amount of Ti/Cr. The addition of a high amount of Cr lead to the formation of chromium clusters on the surface of as-synthesized TiO₂ nanoparticles, and thus the interaction of Cr and TiO₂ becomes feeble. Our XPS results are in very good agreement with our H₂-TPR results (Figure 5) where the strong interaction of Cr and TiO₂ established by the shift of low temperature peak ascribed to the Cr–O–Ti bonding.

The strongly incorporated Cr/TiO₂ catalyst absorbs visible light intensely due to the surface plasmon resonance (SPR) effect.⁴³ Consequently, the surface electrons will be excited and electrons and holes will be separated in the Cr/TiO₂ system by

visible light illumination, which will contribute to the significant improvement in the photoactivity under visible light region.

In addition, the presence of Ti³⁺ sites with narrow band gap is also a factor on enhancing the response of TiO₂. Li et al. stated that the energy level of Ti³⁺ lies between the valence band and the conduction band of TiO₂, which could effectively promote the electrons in the new valence band (VB) to be excited to the conduction band of TiO₂.⁴⁴ The chromium nanoparticles could serve as trapping centers for electrons photoinduced in the conduction band of TiO₂, meanwhile leaving the holes in the valence band of TiO₂. These results imply that the migration of charges is prompted on the interface of metal-doped TiO₂ flame-made nanoparticles and the recombination of photoinduced e⁻/h⁺ pairs is suppressed by the well-known Schottky barrier effect, which will contribute to the enhancement of photocatalytic activity.

Conversely, the anatase-to-rutile ratio changes with Ti/Cr atomic ratio concentration but there is no evidence of precipitation of chromium oxides or chromium titanates by our X-ray diffraction profiles of as-synthesized nanoparticles. Incorporation of Cr into TiO₂ lattice, as proved by XPS, is found to affect the electronic structure of TiO₂, as indicated by the optical spectrophotometry. The impurity band is formed within the forbidden band gap of titanium dioxide which results in the additional absorption within the visible range of the light spectrum. Other researchers also^{45,46} claimed that the lower charge than Ti⁴⁺ compensate not only by oxygen vacancies but also by titanium interstitial ions. Therefore, the substitutional incorporation of chromium into TiO₂ can be expressed, using the Kröger–Vink notation.⁴⁷

3.7. Photocatalytic Performance of M/TiO₂ Catalysts in Visible Region. In the present work, we operated the reactor in plug flow condition where the reactant species are making single pass through the reactor. Here, the independent variable is the molar flow rate and is varied by holding the inlet concentration (C_{A0}) constant and varying the volumetric flow rate. The dependent variable is the fractional conversion. Assuming that the photocatalytic oxidation of acetonitrile follows a power law model, the reactor design equation is (eq 3)

$$\frac{W}{F_{A0}} = \int_{f_{A0}}^{f_A} \frac{df_A}{-r_A} \quad (3)$$

where $-r_A$ is the rate of disappearance of acetonitrile, W is the mass of the catalyst, F_{A0} is the molar flow rate of acetonitrile

entering the reactor, and f_{AO} and f_A are the fractional conversions of A, where $f_{AO} = 0$ and $f_A = 1 - (C_A/C_{AO})$, C_{AO} and C_A inlet and out concentrations of the catalyst. By taking first order photodegradation reaction and integrating the above equation we get (eq 4).

$$\ln(1 - f_A) = -K_A C_{AO} \cdot \frac{W}{F_{AO}} \quad (4)$$

By plotting the graph of $\ln(1 - f_A)$ vs W/F_{AO} we have got the rate constant K_A ($\text{m}^3 \text{g}^{-1} \text{mol}^{-1}$). On the basis of the surface characterization results described above, it is now instructive to compare the photocatalytic activities of all as-prepared metal-doped TiO_2 materials. Figure 9 shows the conversion of

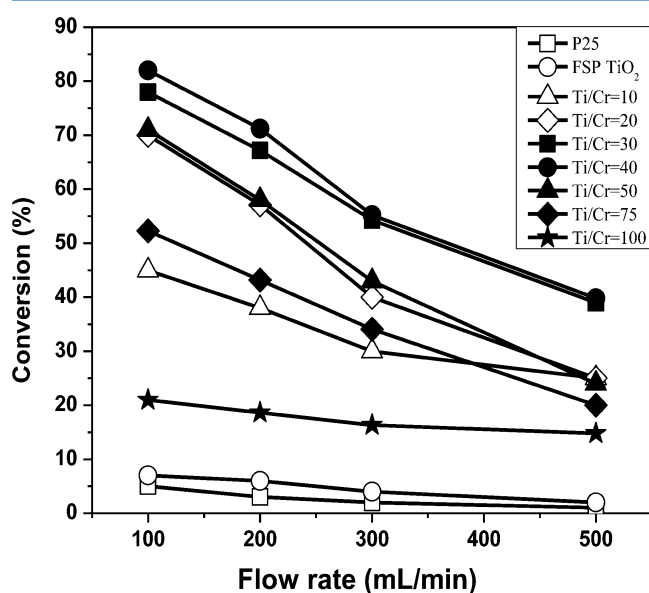


Figure 9. Photocatalytic conversion of acetonitrile over Cr/TiO_2 with the steady 500 ppm concentration of acetonitrile with 60 mg of catalyst loading on to the reactor with respect to different flow.

acetonitrile with respective increasing flow rate values for photo degradation over transition metal incorporated TiO_2 under visible light. We can observe that the Ti/Cr ratio of 40 and 30 catalysts are much more active than the other transition metal incorporated catalysts. The catalyst showed no deactivation usually photo oxidized acetonitrile for a time period of 5 h, because the amount of active oxygen species for oxidation was kept constant during photooxidation. The visible light provided enough energy for the electrons to leap from the valence band to the conduction band and Cr^{6+} acts as an intermediate level for electron excitation under visible light. It is based on the sensitization of titania with a tetrahedrally coordinated transition metal oxide, which can scavenge electrons from the valence band and release electrons to the conduction band upon the excitation by visible light, thus bringing about charge separation. The charges can then react with the adsorbed oxygen and surface hydroxyl groups, producing reactive oxygen species.

Figure 10 shows the photocatalytic conversion of acetonitrile over Cr/TiO_2 for the steady 500 ppm concentration of acetonitrile with 60 mg of catalyst on to the reactor with varying the Cr loading. Not much significant reduction in the concentration of acetonitrile was observed with FSP TiO_2 and P25. In comparison, the activity of TiO_2/Cr increases with

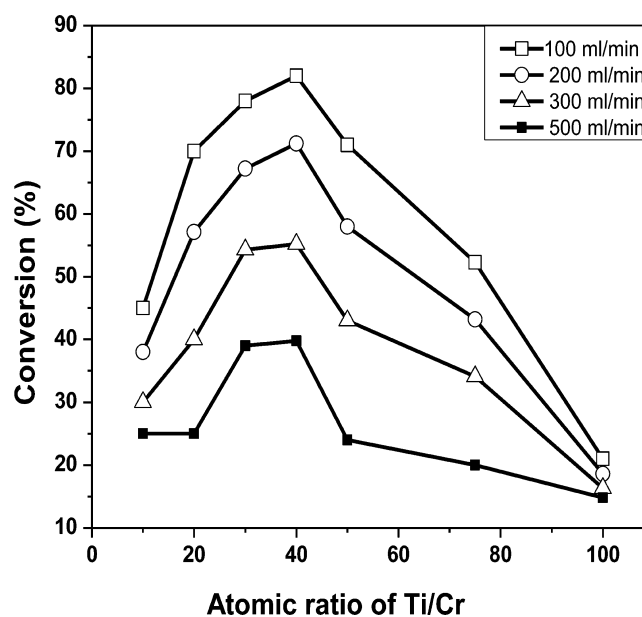


Figure 10. Photocatalytic conversion of acetonitrile over Cr/TiO_2 for continuous 500 ppm concentration of acetonitrile with 60 mg of catalyst onto the reactor surface effect of Cr loading.

decreasing Ti/Cr ratio from 100 to 40. This ratio reaches a maximum at $\text{Ti}/\text{Cr} = 40$ and then decreases with further Cr incorporation. The initial rate increases with the Ti/Cr ratio, namely increasing from 100 to 40, and becomes smaller with the Ti/Cr ratio of 20 and 10 (Table 4). The Figure 10 indicates

Table 4. Photocatalytic Activity and Band-Gap Energies of the Catalyst Used in the Present Study^a

catalyst	UV-vis region	band gap	K ($\text{m}^3 \text{g}^{-1} \text{mol}^{-1}$)
P25	UV	3.11	0.051 ± 0.002
FSP TiO_2	UV	3.08	0.098 ± 0.003
100	visible	2.75	0.050 ± 0.002
75	visible	2.72	0.340 ± 0.010
50	visible	2.69	0.638 ± 0.012
40	visible	2.64	0.812 ± 0.014
30	visible	2.65	0.678 ± 0.013
20	visible	2.63	0.616 ± 0.012
10	visible	2.63	0.210 ± 0.008

^aThe lower activity of TiO_2/Cr with Ti/Cr ratios 100, 75, 50, 20, and 10 indicates that the visible light absorption is only one prerequisite for the catalyst's activity under visible light.

that the activity of $\text{Ti}/\text{Cr} = 40$ is highly related to the Cr^{6+} concentration in the final catalyst, and the Cr^{6+} concentration is the most critical for determining the activity. The previous statement can be seen in the Figure 5, and the TPR studies show that the concentration Cr^{3+} is low for Ti/Cr ratio 30 and 40, and these catalysts mainly contain Cr^{6+} species.

A good correlation is found between the photocatalytic rate and the H_2 consumed corresponding to the first peak of the TPR profiles as shown in Figure 4. In comparison, there is no good correlation between the activity and the total hydrogen consumed for the two reduction peaks in TPR studies. The results above indicate that the interaction of Cr^{6+} with TiO_2 is crucial for a catalyst's activity and the interaction between TiO_2 and Cr^{6+} compared with bulk metal oxides.^{10,11} Therefore, we

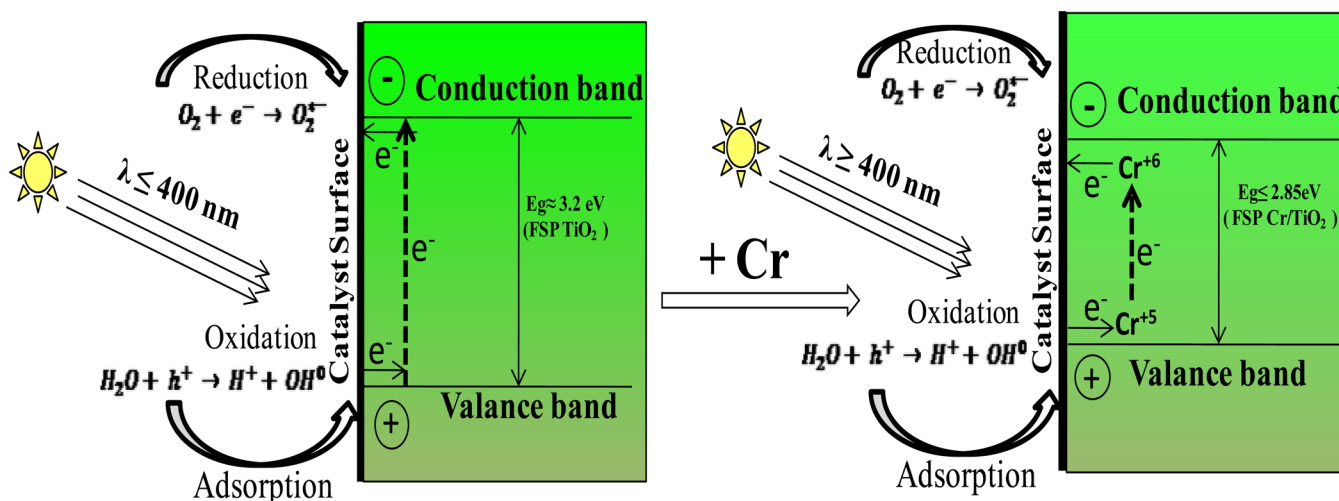


Figure 11. Plausible photocatalytic mechanism of as-prepared Cr incorporated TiO_2 .

conclude that the catalytic activity depends on the catalysts preparation method and the structure of the support material.

From the XPS studies and TPR studies one can clearly observe that the presence of hexavalent chromium is significantly higher than trivalent species contributes to the activity of the catalyst. This will lead to a conclusion that Cr^{6+} is the species primarily responsible for the photoactivity in visible light. These results are in agreement with the reported literature.^{10,11,16,36,48–50} Figure 11 elucidates the proposed mechanism of the charge generation happening at the heterojunction of the loaded titania with chromium. Such a transition, when it occurs in contact with TiO_2 , can produce an effect similar to that found in platinum(IV) chloride modified titania.⁵⁰

The strong interaction (formation of $\text{Cr}-\text{O}-\text{Ti}$ bonds) and the synchronization of Cr and TiO_2 allows for a unique transition under visible light excitation, $\text{Cr}^{6+}=\text{O}^{2-} \rightarrow \text{Cr}^{5+}-\text{O}^{1-}$,^{10,51} and is essential for the activity of a photocatalyst under visible light. In the current plausible mechanism (Figure 11), a strong oxidant (hole) can be generated when Cr^{6+} ion excites under visible light absorption which is due to the Cr^{6+} anion undergoing the ligand-to-metal charge transfer (LMCT) excitation.⁵² Simultaneously, the oxidation reaction of the water takes place at the generated hole where an electron is produced which is used by Cr^{6+} to form Cr^{5+} . The Cr^{5+} probably contributes an electron into the neighboring TiO_2 , and the reduction reaction of the O_2 takes place on the surface where O_2^{2-} can scavenge an electron from the surface of the catalyst. The formation of surface hydroxyl radicals and oxygen species (O_2^{2-}) occurs due to the oxidation reaction and scavenging of the electron from the surface, respectively. The formed hydroxyl radicals and labile oxygen species (O_2^{2-}) will further react with the acetonitrile molecule and produce the corresponding minerals hence degrading the acetonitrile. The active radicals will react with the acetonitrile and produce the corresponding minerals hence degrading the acetonitrile.

4. CONCLUSIONS

The Cr-incorporated TiO_2 catalyst is highly active for the gas phase photodegradation of acetonitrile under visible light. The optimum atomic ratio of Ti to Cr in the catalyst is 40. The activity of the catalysts monotonically increases with the Cr concentration up to the optimum amount of Cr in the catalyst.

However, the activity decreases abruptly with further Cr incorporation due to the decreasing Cr^{6+} concentration in the catalyst. Cr^{6+} is the dominant form of chromium in Cr/TiO_2 with Ti/Cr ratios of 40 and 30. Mixed chromium oxides (Cr^{6+} and Cr^{3+}) form in the samples with Ti/Cr less than 30 due to the destruction of abundance of the Cr ions. Cr^{6+} , instead of Cr^{3+} , is found to be the active form. The catalyst's activity is highly related to the presence of Cr^{6+} concentration. The characterization and performance studies show that the interaction of Cr^{6+} with TiO_2 is crucial for the catalyst's activity. The interaction of Cr^{6+} and TiO_2 allows for a special transition under visible light, $\text{Cr}^{6+}=\text{O}^{2-} \rightarrow \text{Cr}^{5+}-\text{O}^{1-}$, and is essential for the activity of a photocatalyst under visible light. The peak position for Ti 2p in the Cr/TiO_2 sample shifted to higher binding energies than that of bare TiO_2 , and the Cr 2p peak shifted to lower binding energies. These shifts suggest a lower electron density of the TiO_2 surface after chromium nanoparticles incorporation, and strong interaction between Cr species and TiO_2 nanostructure in the interface of flame-made nanoparticles with a Ti/Cr atomic ratio equal to 40. The plausible mechanism of the photodegradation in visible light on Cr/TiO_2 made by flame aerosol pyrolysis is proposed.

■ ASSOCIATED CONTENT

Supporting Information

Schematic representation of the experimental setup, schematic representation of the gas phase visible light photocatalytic reactor setup, and deconvoluted reduction peaks of Cr doped titania catalysts made by FSP synthesis technique using different Ti/Cr atomic ratios. This material is available free of charge via the Internet at <http://pubs.acs.org>.

■ AUTHOR INFORMATION

Corresponding Authors

*E-mail: makram.suidan@uc.edu; msuidan@aub.edu.lb.

*Tel.: (513) 556-1474. Fax: (513) 556-3473. E-mail: panagiotis.smirniotis@uc.edu.

Author Contributions

The manuscript was written through contributions of all authors. All authors have given approval to the final version of the manuscript.

Notes

The authors declare no competing financial interest.

ACKNOWLEDGMENTS

The authors wish to acknowledge EPA/Pegasus contract (Contract No. EP-C-11-006) for financial support of this work through the scholarship to Siva Nagi Reddy Inturi.

REFERENCES

- (1) Fujishima, A.; Honda, K. Electrochemical Photolysis of Water at a Semiconductor Electrode. *Nature* **1972**, *238*, 37–38.
- (2) Fox, M. A.; Dulay, M. T. Heterogeneous Photocatalysis. *Chem. Rev.* **1993**, *83*, 341–357.
- (3) Hoffmann, M. R.; Martin, S. T.; Choi, W.; Bahnemann, D. W. Environmental Applications of Semiconductor Photocatalysis. *Chem. Rev.* **1995**, *95*, 69–96.
- (4) Linsebigler, A. L.; Lu, G.; Yates, J. T. Photocatalysis on TiO_n Surfaces: Principles, Mechanisms, and Selected Results. *Chem. Rev.* **1995**, *95*, 735–758.
- (5) Dvoranova, D.; Brezova, V.; Mazur, M.; Malati, M. A. Investigations of Metal-doped Titanium Dioxide Photocatalysts. *Appl. Catal., B* **2002**, *37*, 91–105.
- (6) Iwasaki, M.; Hara, M.; Kawada, H.; Tada, H.; Ito, H. S. Cobalt Ion-Doped TiO_2 Photocatalyst Response to Visible Light. *J. Colloid Interface Sci.* **2000**, *224*, 202–204.
- (7) Xu, Y. M.; Langford, C. H. Enhanced Photoactivity of a Titanium(IV) Oxide Supported on ZSMS and Zeolite A at Low Coverage. *J. Phys. Chem.* **1995**, *99*, 11501–11507.
- (8) Choi, W.; Termin, A.; Hoffmann, M. R. The Role of Metal Ion Dopants in Quantum-Sized TiO_2 : Correlation between Photo-reactivity and Charge Carrier Recombination Dynamics. *J. Phys. Chem.* **1994**, *98*, 13669–13679.
- (9) Serpone, N.; Lawless, D.; Disdier, J.; Herrmann, J. M. Spectroscopic, Photoconductivity, and Photocatalytic Studies of TiO_2 Colloids: Naked and with the Lattice Doped with Cr^{3+} , Fe^{3+} , and V^{5+} Cations. *Langmuir* **1994**, *10*, 643–652.
- (10) Davydov, L.; Reddy, E. P.; France, P.; Smirniotis, P. G. Transition-Metal-Substituted Titania-Loaded MCM-41 as Photocatalysts for the Degradation of Aqueous Organics in Visible Light. *J. Catal.* **2001**, *203*, 157–167.
- (11) Reddy, E. P.; Sun, B.; Smirniotis, P. G. Transition Metal Modified TiO_2 -Loaded MCM-41 Catalysts for Visible- and UV-Light Driven Photodegradation of Aqueous Organic Pollutants. *J. Phys. Chem. B* **2004**, *108*, 17198–17205.
- (12) Borgarello, E.; Kiwi, J.; Gratzel, M.; Pelizzetti, E.; Visca, M. Visible Light Induced Water Cleavage in Colloidal Solutions of Chromium-Doped Titanium Dioxide Particles. *J. Am. Chem. Soc.* **1982**, *104*, 2996–3002.
- (13) Anpo, M. Preparation, Characterization, and Reactivities of Highly Functional Titanium Oxide-Based Photocatalysts able to Operate under UV-visible Light Irradiation: Approaches in Realizing High Efficiency in the use of Visible Light. *Bull. Chem. Soc. Jpn.* **2004**, *72*, 1427–1442.
- (14) Anpo, M.; Takeuchi, M. The Design and Development of Highly Reactive Titanium Oxide Photocatalysts Operating under Visible Light Irradiation. *J. Catal.* **2003**, *216*, 505–516.
- (15) Yamashita, H.; Harada, M.; Misaka, J.; Takeuchi, M.; Neppolian, B.; Anpo, M. Photocatalytic degradation of Organic Compounds Diluted in Water using Visible Light-Responsive Metal Ion-Implanted TiO_2 Catalysts: Fe Ion-Implanted TiO_2 . *Catal. Today* **2003**, *84*, 191–196.
- (16) Sun, B.; Reddy, E. P.; Smirniotis, P. G. Effect of the Cr^{6+} Concentration in Cr-Incorporated TiO_2 -loaded MCM-41 Catalysts for Visible Light Photocatalysis. *Appl. Catal. B: Environ.* **2005**, *57*, 139–149.
- (17) Madler, L. Liquid-fed Aerosol Reactors for One-step Synthesis of Nano-structured Particles. *KONA* **2004**, *22*, 107–120.
- (18) Strobel, R.; Baiker, A.; Pratsinis, S. E. Aerosol Flame Synthesis of Catalysts. *Adv. Powder Technol.* **2006**, *17*, 457–480.
- (19) Pratsinis, S. E. Flame Aerosol Synthesis of Ceramic Powders. *Prog. Energ. Combust.* **1998**, *24*, 197–219.
- (20) Madler, L.; Kammler, H. K.; Mueller, R.; Pratsinis, S. E. Controlled Synthesis of Nanostructured Particles by Flame Spray Pyrolysis. *Aerosol Sci.* **2002**, *33*, 369–389.
- (21) Teoh, W. Y.; Madler, L.; Beydoun, D.; Pratsinis, S. E.; Amal, R. Direct (One-Step) Synthesis of TiO_2 and Pt/ TiO_2 Nanoparticles for Photocatalytic Mineralisation of Sucrose. *Chem. Eng. Sci.* **2005**, *60*, 5852–5861.
- (22) Byrd, G.; Fowler, K.; Hicks, R.; Lovette, M.; Borgerding, M. Isotope Dilution Gas Chromatography-Mass Spectrometry in the Determination of Benzene, Toluene, Styrene and Acrylonitrile in Mainstream Cigarette Smoke. *J. Chromatogr. A.* **1990**, *503*, 359–436.
- (23) Sing, K. S. W.; Everett, D. H.; Haul, R. A.W.; Moscou, L.; Pierotti, R. A.; Rouquerol, J.; Siemieniewska, T. Reporting Physisorption Data for Gas/Solid Systems with Special Reference to the Determination of Surface Area and Porosity. *Pure Appl. Chem.* **1985**, *57*, 603–619.
- (24) Falong, J.; Yan, H.; Yiwen, T.; Lizhi, Z. A General Non Aqueous Sono Electrochemical Approach to Nanoporous Zn and Ni particles. *Powder Technol.* **2007**, *176*, 130–136.
- (25) Jinyou, L.; Yanwei, S.; Bin, D.; Jianmao, Y.; Jianyong, Y.; Salem, S. A. D. Nanoporous Polystyrene Fibers for Oil Spill Cleanup. *Mar. Pollut. Bull.* **2012**, *64*, 347–352.
- (26) Jesse, J. W.; Julio, J. L.; Isabel, T. T.; Marc, A. A. Low Surface Area Carbon Fiber Electrodes Coated with Nanoporous Thin-Films of $\gamma\text{-Al}_2\text{O}_3$ and SiO_2 : Relationship between Coating Conditions, Microstructure and Double Layer Capacitance. *J. Electrochem. Soc.* **2012**, *159*, A1374–A1382.
- (27) Jenkins, R.; Snyder, R. L. *Introduction to X-ray Powder Diffractometry*; Wiley & Sons, Inc.: New York, 1996.
- (28) Biswajit, C.; Amarjyoti, C. Structural, Optical and Ferromagnetic Properties of Cr doped TiO_2 Nanoparticles. *Mater. Sci. Eng. B* **2013**, *178*, 794–800.
- (29) Zhu, J. F.; Chen, F.; Zhang, J. L.; Chen, H. J.; Anpo, M. Fe^{3+} - TiO_2 Photocatalysts Prepared by Combining Sol-Gel Method with Hydrothermal Treatment and Their Characterization. *J. Photochem. Photobiol. A, Chem.* **2006**, *180*, 196–204.
- (30) Paruchai, P.; Burapat, I.; Khatcharin, W.; Sukon, P.; Natda, W. Highly Efficient Visible-Light-Induced Photocatalytic Activity of Fe-doped TiO_2 Nanoparticles. *Eng. J.* **2012**, *16*, 144–151.
- (31) Hui, L.; Linlin, Z.; Jong, P. K.; Sou, H. S.; Jung, H. P. Perovskite $\text{La}_{0.6}\text{Sr}_{0.4}\text{B}_{0.2}\text{Fe}_{0.8}\text{O}_{3-\delta}$ (B = Ti, Cr, Co) Oxides: Structural, Reduction-Tolerant, Sintering, and Electrical Properties. *Solid State Ionics* **2012**, *209–210*, 24–29.
- (32) Sun, B.; Reddy, E. P.; Smirniotis, P. G. Visible Light Cr(VI) Reduction and Organic Chemical Oxidation by TiO_2 Photocatalysis. *Environ. Sci. Technol.* **2005**, *39*, 6251–6259.
- (33) Nahar, S.; Hasegawa, K.; Kagaya, S. Photocatalytic Degradation of Phenol by Visible Light-Responsive Iron-doped TiO_2 and Spontaneous Sedimentation of the TiO_2 Particles. *Chemosphere* **2006**, *65*, 1976–1982.
- (34) Klosek, S.; Raftery, D. Visible Light Driven V-Doped TiO_2 Photocatalyst and Its Photooxidation of Ethanol. *J. Phys. Chem. B* **2001**, *105*, 2815–2819.
- (35) Rahman, A.; Ahmed, M. Dehydration of Propane over Chromia/Alumina: A Comparative Characterization Study of Fresh and Spent Catalysts. *Catal. Petrol. Refin. Petrochem. Ind.* **1995**, *100*, 419–426.
- (36) Liu, G.; Yang, H. G.; Wang, X.; Cheng, L.; Lu, H.; Wang, L.; Lu, G. Q.; Cheng, H. -M. Enhanced Photoactivity of Oxygen-Deficient Anatase TiO_2 Sheets with Dominant {001} Facets. *J. Phys. Chem. C* **2009**, *113*, 21784–21788.
- (37) Jiang, B.; Tian, C.; Pan, Q.; Jiang, Z.; Wang, J. Q.; Yan, W.; Fu, H. Enhanced Photocatalytic Activity and Electron Transfer Mechanisms of Graphene/ TiO_2 with Exposed {001} Facets. *J. Phys. Chem. C* **2011**, *115*, 23718–23725.
- (38) Wang, W.; Lu, C.; Ni, Y.; Xu, Z. Crystal Facet Growth Behavior and Thermal Stability of {001} Faceted Anatase TiO_2 : Mechanistic Role of Gaseous HF and Visible-Light Photocatalytic Activity. *Cryst. Eng. Comm.* **2013**, *15*, 2537–2543.

(39) Gonbeau, D.; Guimon, C.; Pfister-Guillouzo, G.; Levasseur, A.; Meunier, G.; Dormoy, R. XPS Study of Thin Films of Titanium Oxysulfides. *Surf. Sci.* **1991**, *254*, 81–89.

(40) Sreekanth, P. M.; Smirniotis, P. G. Selective Reduction of NO with CO over Titania Supported Transition Metal Oxide Catalysts. *Catal. Lett.* **2008**, *122*, 37–42.

(41) Su, C.; Liu, L.; Zhang, M.; Zhang, Y.; Shao, C. Fabrication of Ag/TiO₂ Nano Hetero Structures with Visible Light Photocatalytic Function via a Solvothermal Approach. *Cryst. Eng. Comm.* **2012**, *14*, 3989–3999.

(42) Wang, Y. X.; Liu, H.; Li, Z. Q.; Zhang, X. X.; Zheng, R. K.; Ringer, S. P. Role of Structural Defects on Ferromagnetism in Amorphous Cr-doped TiO₂ Films. *Appl. Phys. Lett.* **2006**, *89*, 042511–042511–3.

(43) Chien, H. H.; Wu, H. C. Fabrication of Size-Tunable Hierarchical porous Cr Nanoring Arrays by Modified Nanosphere Lithography. *Micro Nano Lett.* **2012**, *7*, 1033–1037.

(44) Li, J. X.; Xu, J. H.; Dai, W. L. Dependence of Ag Deposition Methods on the Photocatalytic Activity and Surface State of TiO₂ with Twistlike Helix Structure. *J. Phys. Chem. C* **2009**, *113*, 8343–8349.

(45) Kofstad, P. Note on the Defect Structure of Rutile TiO₂. *J. Less-Common Met.* **1967**, *13*, 635–638.

(46) Nowotny, J.; Radecka, M.; Rekas, M. Semiconducting Properties of undoped TiO₂. *J. Phys. Chem. Solids* **1997**, *58*, 927–937.

(47) Trenczek-Zajac, A.; Radecka, M.; Jasinski, M.; Michalow, K. A.; Rekas, M.; Kusior, E.; Zakrzewski, K.; Heel, A.; Graule, T.; Kowalski, K. Influence of Cr on Structural and Optical Properties of TiO₂:Cr Nanopowders Prepared by Flame Spray Synthesis. *J. Power Sources* **2009**, *194*, 104–111.

(48) Herrmann, J. M. Fundamentals and Misconceptions in Photocatalysis. *J. Photochem. Photobiol. A, Chem.* **2010**, *216*, 85–93.

(49) Sun, B.; Reddy, E. P.; Smirniotis, P. G. TiO₂-Loaded Cr-Modified Molecular Sieves for 4-Chlorophenol Photodegradation under Visible Light. *J. Catal.* **2006**, *237*, 314–321.

(50) Zang, L.; Lange, C.; Abraham, I.; Storck, S.; Maier, W.; Kisch, H. Amorphous Microporous Titania Modified with Platinum(IV) Chlorides-A New Type of Hybrid Photocatalyst for Visible Light Detoxification. *J. Phys. Chem. B* **1998**, *102*, 10765–10771.

(51) Joanna, K.; Przemysław, Z.; Krzysztof, K.; Konrad, S.; Wojciech, M. Photocatalysis Involving a Visible Light-Induced Hole Injection in a Chromate(VI)–TiO₂ System. *J. Phys. Chem. C* **2012**, *116*, 21762.

(52) Cruywagen, J. J.; Heyns, J. B. B.; Rohwer, E. A. New Spectrophotometric Evidence for the Existence of HCrO₄[−]. *Polyhedron* **1998**, *17*, 1741–1746.